Revista Mexicana de Física
ISSN: 0035-001X
rmf@ciencias.unam.mx
Sociedad Mexicana de Física A.C.
México

Garza-Navarro, M.A.; González, V.; Hinojosa, M.; Torres-Castro, A.
Preparation of chitosan/magnetite polymeric-magnetic films
Revista Mexicana de Física, vol. 57, núm. 2, abril-, 2011, pp. 51-56
Sociedad Mexicana de Física A.C.
Distrito Federal, México

Preparation of chitosan/magnetite polymeric-magnetic films

M.A. Garza-Navarro[a,b], V. González[a,b], M. Hinojosa[a,b], and A. Torres-Castro[a,b]
[a]*Facultad de Ingeniería Mecánica y Eléctrica, Universidad Autónoma de Nuevo León, Universidad Ave. S/N, San Nicolás de los Garza, Nuevo León 66450, México.*
[b]*Centro de Innovación, Investigación y Desarrollo en Ingeniería y Tecnología, Universidad Autónoma de Nuevo León, Apodaca, Nuevo León 66600, México,*
Phone: +52 (81) 8329-4000 x 5770
e-mail: alejandro.torrescs@uanl.edu.mx

Recibido el 29 de enero de 2009; aceptado el 14 de julio de 2010

Based on a solid state in situ co-precipitation process, it was developed a method to obtain nanocomposites of chitosan/magnetite with high magnetite content (75 wt%) and narrow particles size distribution which observe a mean diameter of about 7 nm. The possibility to obtain high magnetite concentration and the observed invariance of size distribution with magnetite content, differentiate this method with others reported in the literature. The nanocomposites were structurally and morphological studied by X-ray diffraction and transmission electron microscopy, and magnetically characterized by magnetometry. The nanocomposites show a congruent behaviour with the actual magnetic theory on single domain particles, presenting superparamagnetic character at room temperature and ferromagnetic properties at 2 K.

Keywords: Magnetite; nanoparticles; superparamagnetism; polymeric films.

En este trabajo se reporta el desarrollo de materiales nanocompósitos de nanopartículas de magnetita sintetizadas mediante una reacción de co-precipitación *in situ* en estado sólido utilizado como matriz al biopolímero quitosán. A diferencia de otras rutas de síntesis reportadas en la literatura, la metodología propuesta en este trabajo asegura una distribución estrecha de tamaño de partícula, cuyo diámetro promedio es de 7 nm, aun a concentraciones de nanopartículas en el nanocompósito tan altas como 75% en peso de nanopartículas con respecto al peso total del nanocompósito. Los nanocompósitos obtenidos fueron estudiados estructural y morfológicamente por técnicas de difracción de rayos X y microscopía electrónica de transmisión, y sus características magnéticas fueron evaluadas por magnetometría. Los nanocompósitos sintetizados muestran un comportamiento magnético coherente con el reportado para partículas magnéticas monodominio, presentando superparamagnetismo a temperatura ambiente y características ferromagnéticas a 2 K.

Descriptores: Magnetita; nanopartículas; superparamagnetismo; películas poliméricas.

PACS: 75.20.-g; 75.30.-m; 75.47.Lx; 75.50.Dd; 75.50.Tt

1. Introduction

Superparamagnetic nanocomposites represent an important class of new advanced materials with possible applications as magnetic drug carriers, hyperthermia local inductors for cancer therapy, magnetic cell separators and biological sensors [1-6]. Important developments have been reported in the synthesis of drug targeting delivery systems, in which particles of metal oxides are embedded in biocompatible and biodegradable polymeric matrices [7-9]. Accordingly, has been theorized that once these composite systems are introduced into the blood vessel, it is possible to drive the magnetic drug carriers through the body using an external magnetic field, in order to deliver drug molecules to targeted organs [10,11]. Development of nanoparticles systems for hyperthermia has been also reported [2,12,13]. These systems should be operable using an AC magnetic field to induce alternating spin magnetic moments response at each superparamagnetic particle in colloidal suspension. Hence, local heating is produced to ablate cancerous tissues [2]. The use of composites materials for cell separation and biological sensing processes has been also discussed [5,6]. This kind of systems are composed by magnetic nanostructures coated with biocompatible surfactants capable to interact with biological entities such as red blood cells, bacteria, lung cancer cells, urological cancer cells and Glogi vesicles [14-16]. It is possible the identification of added biological molecules onto magnetic nanoparticles through the study of its dynamic magnetic properties [6].

Several approaches have been suggested to the synthesis of iron oxide nanoparticles in polymeric matrices using *in situ* chemical co-precipitation [17-20]. For example, Z. Huang *et al*. have reported the synthesis of polystyrene-coated magnetite microparticles during its polymerization reaction, obtaining magnetite nanoparticles with sizes between 10 to 65 nm, depending on the magnetite concentration, which is as high as 58 wt% [19]. D. Rabelo *et al*. have reported that it is possible to obtain magnetite nanoparticles by the *in situ* oxidation of adsorbed Fe^{2+} in a mesoporous poly-(styrene-co-divinyl-bencene) template, and a subsequent co-precipitation of ferric and ferrous ions, obtaining magnetite nanoparticles coated with the polymer at magnetite concentration as high as 3.6 wt% and particle sizes between 20 and 50 nm [20]. It is important to remark that in these approaches have been established that the increases of magnetite concentration conduces to an increases of the particle size. Specifically, the synthesis of chitosan/magnetite nanocomposites has been performed by two steps procedures, as is reported elsewhere [21-24]. Briefly, these approaches consider the synthesis of magnetite nanoparticles followed by its dispersion into chitosan acid dissolutions,

giving chitosan/magnetite nanocomposites with a particle sizes interval of 14 to 1390 nm, depending on the chitosan/magnetite weight content ratio, which has been reported as high as 4 [21-24].

According to previous reports, the polyamine-saccharide chitosan presents a remarkable affinity to form coordination compounds between its amine and hydroxyl functional groups and metal ions, such as Fe(II), Fe(III), Co(II), Cu(II), Ni(II), Pb(II), Cd(II) and Cd(IV) [25-32]. Therefore, the synthesis of chitosan/magnetite nanocomposites could be possible from coordinated compounds between ferric and ferrous ions, and chitosan, as some authors have suggested previously [33,34]. Thereby, considering the existent works about the development of chitosan/magnetite nanocomposites and those related to *in situ* co-precipitation of magnetite in polymeric matrices, in this work we report the synthesis of chitosan/magnetite polymeric-magnetic nanocomposites films using *in situ* chemical co-precipitation of coordinated ferric and ferrous ions in a chitosan matrix. It is important to remark that, unlike to previous reports, the proposed synthetic route gives narrow particle size distribution even at nanoparticles concentration as high as 75 wt%.

2. Experimental

2.1. Materials

All reagents, $FeCl_2$-$4H_2O$, $FeCl_3$-$6H_2O$, NaOH, HCOOH (88 %v) and low molecular weight chitosan (degree of deacetylation of 84.5% and molecular weight of 50-190 kDa) were acquired as reactive grade from Aldrich Co., and used as received without further treatment.

2.2. Synthesis

Ferric and ferrous chlorides were dissolved in formic acid to give stoichiometric ratio of 2:1 of Fe(III):Fe(II) and concentrations of 0.034M of salts, under magnetic stirring at room conditions. The dissolution was mixed with a previously formed dissolution of low molecular weight chitosan in formic acid at concentration of 10.0 mg/mL. The amount of each dissolution was mixed at the necessary proportions to obtain chitosan/magnetite nanocomposites samples with weight ratios of 75/25, 50/50 and 25/75 w/w, which were namely as 75C25M, 50C50M and 25C75M, respectively. The dissolutions were placed in Petri dishes and the dissolvent was evaporated at room temperature. The resulting yellowish to orange films was immersed into 5 M aqueous dissolution of NaOH. The films turn dark-brownish indicating the *in situ* co-precipitation of the iron oxide. The films were washed several times with de-ionized water and finally dried at room temperature.

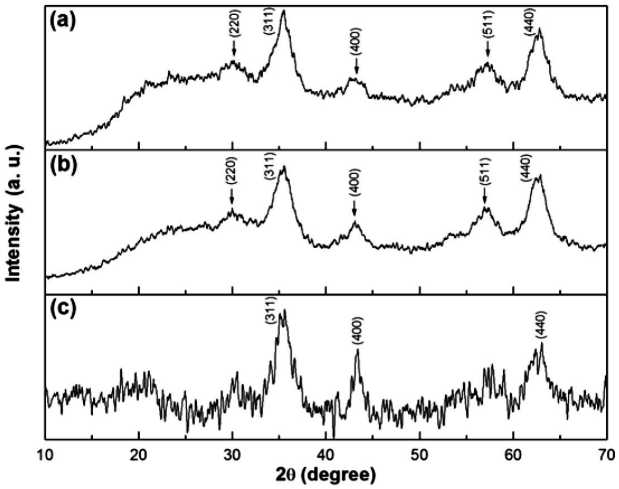

FIGURE 1. XRD patterns obtained from the nanocomposite samples: (a) 75C25M, (b) 50C50M and (c) 25C75M.

2.3. Characterization

Nanocomposites were analyzed by X-ray diffraction (XRD) of powdered samples using a Phillips multipurpose X-ray diffractometer with CuK-α radiation. Transmission electron microscopy (TEM) was performed in a Jeol 2010F using an acceleration voltage of 200.0 kV; the TEM specimens were prepared dispersing the chitosan/magnetite powder in isopropanol using an ultrasonic bath and placing an aliquot of the dispersion onto a lacey-carbon-coated grid. The magnetic properties of the nanocomposites were determined using a superconducting quantum interference device (SQUID) MPMS-5 (Quantum Design) magnetometer. Magnetization applied field-dependent, M(H), curves were obtained at 300.0 K and 2.0 K, using in both cases a maximum applied magnetic field of 1 T. Magnetization temperature-dependent, M(T), curves were obtained performing zero field cooled (ZFC) and field cooled (FC) magnetization processes from 2.0 K to 300.0 K at 10.0 mT.

3. Results and discussion

3.1. Crystalline and morphological characterization

The XRD patterns of the three nanocomposite samples are shown in Fig. 1. The observed patterns are consistent with those reported for magnetite [JCPDS 19-0629 diffraction card] and maghemite [JCPDS 39-1346 diffraction card]. The amorphous halo between 10° and 28° could be attributed to the chitosan matrix, as has been documented elsewhere [35]. The broadening of the diffraction peaks makes difficult to precise if the reflecting planes corresponds to magnetite or maghemite. However, the absence of the corresponding diffraction peaks of (211) at 32.2° indicates the absence of a separate cubic maghemite phase [see JCPDS 39-1346 diffraction card]. The presence of a tetragonal maghemite phase is

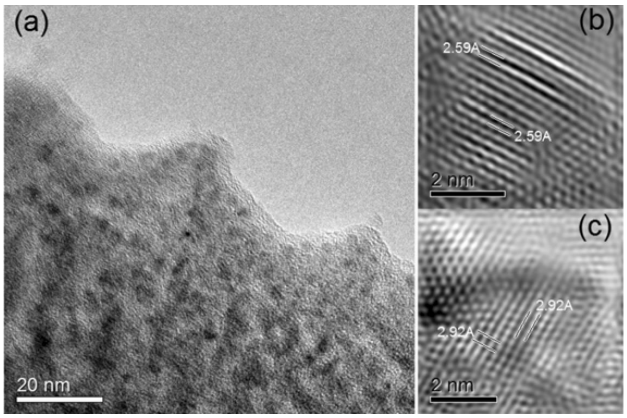

FIGURE 2. TEM images obtained from the nanocomposite samples: (a) 50C50M, (b) 75C25M and (c) 25C75M.

not clearly detectable, since the corresponding peaks attributed to the planes (203) and (116) at 23.9° and 26.2°, respectively, are obscured by the amorphous halo in this interval [see JCPDS 25-1402 diffraction card].

In order to identify the embedded phase in the chitosan matrix, we calculated the lattice parameter using the peaks corresponding to (311) and (400) reflecting planes. The results of these calculations were 8.36 and 8.37 Å for the samples 25C75M, 50C50M and 75C25M, respectively. Note that these results are close to the reported lattice parameter for magnetite and cubic maghemite: 8.396 Å and 8.352 Å, respectively. This could be attributed to a partial oxidation of Fe(II) to Fe(III). Since the ionic radius of Fe(II) cation (0.074 nm) is bigger than that of Fe(III) (0.064 nm), an increase in Fe(III) content due to oxidation of Fe(II) will reduce the size of the unit cell. Accordingly, the major decrease in Fe(II) content is shown by 025C075M sample. Thus, it is reasonable to assume that the polymer matrix interferes, avoiding oxidation. This effect has been reported previously for chitosan/magnetite hydrogels [33]. Moreover, in all cases partial oxidation occurs and hence the crystalline structure of the dispersed phase is composed of non-stoichiometric magnetite [36].

The dimension of the crystalline domains of the particles can be estimated from the broadening of the Bragg diffraction lines using the Scherrer equation as follows:

$$L = \frac{K\lambda}{\beta \cos\theta} \tag{1}$$

here L is the volume weighted average crystal size, K is the Scherrer factor (usually taken as 0.89), λ is the X-ray wavelength, β is the mean width of the maximum peak and θ is the Bragg angle of the diffraction. The results of these calculations give crystalline domains sizes of 4.64, 4.91 and 5.45 nm for the samples 25C75M, 50C50M and 75C25M, respectively. Here it is noticeable small crystal domains sizes even at nanoparticles weight content ratio of 75 % w/w, which could be explained as a stabilization feature of the chitosan matrix. Nevertheless, in order to associate the crystal domain sizes with the particle sizes, it is necessary to observe the morphology and crystalline ordering of the magnetite nanoparticles.

The morphology and crystalline ordering of the magnetite nanoparticles is shown in the Fig. 2. Figure 2a shows the presence of well dispersed and stabilized 4 nm magnetite nanoparticles from sample 50C50M, which is embedded in the chitosan matrix. Figures 2b and 2c shows high resolution images of particles, obtained from the samples 75C25M and 25C75M samples, respectively. Here is clearly observed a regular array of atomic site, which does not presents any disruption associated with crystalline faults (ex. grain boundaries). The interplanar spacing measures at Figs. 2b and 2c indicates that this arrangement corresponds to the family planes $\{311\}$ and $\{220\}$, respectively, of magnetite [see JCPDS 19-0629 diffraction card]. Thus, considering this feature, we can assure that magnetite nanoparticles are single crystals and hence its particle size is proportional to the size of its crystalline domains.

From these results is possible to state that particle size is controlled by two factors: 1) the reactants concentration and 2) the steric effect of the stabilization media, given by intermolecular sites used to nucleate the magnetite nanoparticles, due to the coordination of the reactants with its amine and hydroxyl functional groups. Therefore, if the concentration of the reactants is controlled in order to obtain nanocomposites with a given nanoparticles weight content, the final dimensions will depend of the size of the intermolecular sites where particles growth take place.

3.2. Magnetic measurements

The Fig. 3 shows the hysteresis loops, M(H), obtained from the nanocomposites samples 75C25M, 50C50M and 25C75M. As it is displayed in the Fig. 3a, at 2 K all samples depict typical ferromagnetic behavior, with coercivities of 41.8, 44.8 and 47.7 mT, remanences of 20.0, 16.3 and 9.4 A-m^2/kg, and saturation of 67.2, 65.4 and 49.4 A-m^2/kg, respectively; saturation of the samples was deduced from linear extrapolation of the initial magnetization curves to infinite field. From this data is possible to indicate that remanence ratio of all nanocomposite samples is smaller than the reported for isolated magnetic particles systems with uniaxial anisotropy, 0.5, or cubic anisotropy, 0.8, suggesting that the response of the spin magnetic moment of particles is leaded by the competition between interparticle and intraparticle interactions [34,37,38]. Moreover, the saturation value of the nanocomposites is lower than the reported for bulk magnetite of 100 A-m^2/kg [39]. This lack of saturation could be associated to surface effects due to the particle size [40]. It is well know that ferrimagnetic order in oxides nanoparticles can deviate from the conventional picture of two sublattices which couple each other by superexchange interactions, to a more complex ordering where canted spins onto particles surface interact with co-lineally ordered spins of its core [41,42]. The canting of the surface spins could be explained as the result of the incomplete coordination of the surface cations due to the

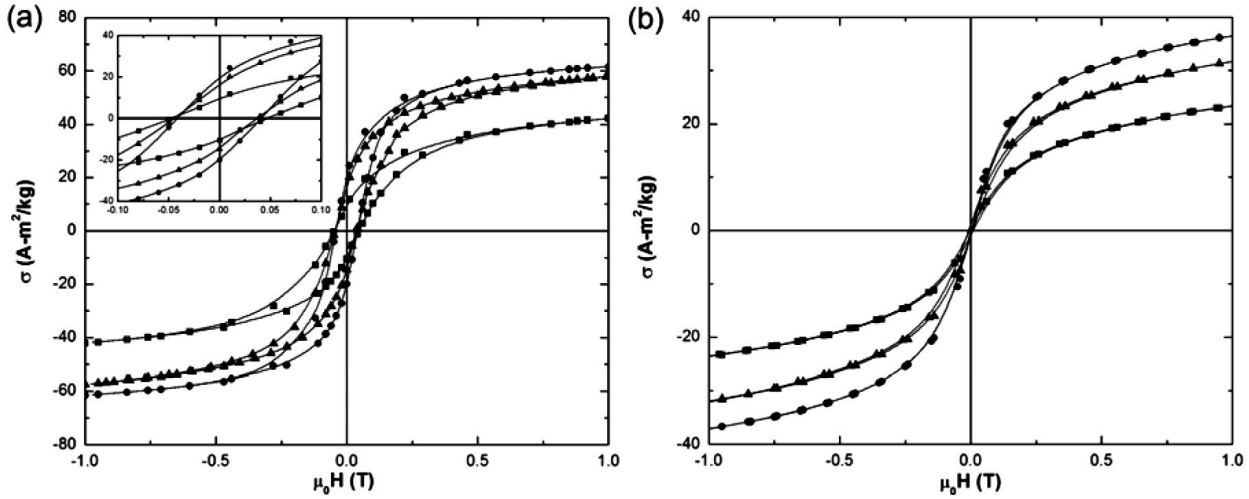

FIGURE 3. Hysteresis loop obtained from the samples 75C25M (●) 50C50M (▲) and 25C75M (■) at (a) 2 K and (b) 300 K. The units of the inset axis at (a) are the same than that showed in the graphs.

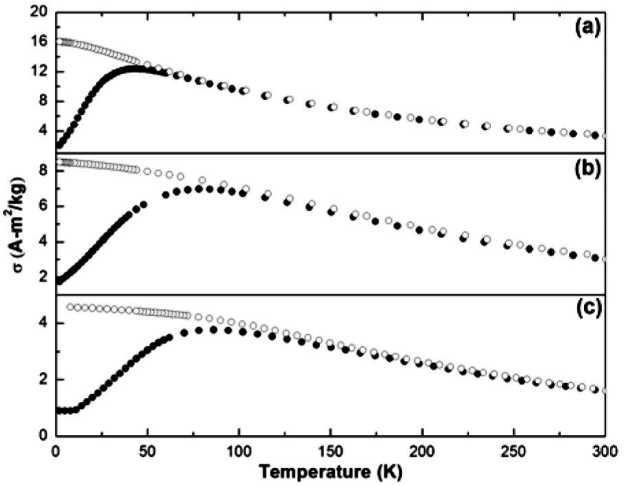

FIGURE 4. Magnetization temperature-dependent curves obtained from ZFC (solid circles) and FC (open circles) measurements at 10 mT to the samples: (a) 75C25M, (b) 50C50M and (c) 25C75M.

reduction of the particle size or the presence of vacancies in the crystalline structure [42].

The Fig. 3b shows the M(H) curves recorded from nanocomposites samples at 300 K. These curves depict typical magnetic response of magnetic nanoparticles under superparamagnetic regimen, which is characterized by the absence of hysteretic features. The superparamagnetic response is manifested by single domain particles systems when its magnetic properties are measured above certain critical temperature from which its ferromagnetic frozen ordering diverges to a fluctuating spin ordering regimen [41,43-44]. This temperature is called blocking temperature, T_B, and can be approximated as the threshold where the thermal energy overcome the energy barrier related to the change in the orientation of the spin magnetic moment of a particle or an assembly of particles [44,45].

The Fig. 4 shows the magnetization temperature-dependent, M(T), ZFC and FC curves of the nanocomposites samples. As it is noticeable, ZFC curves depict an increase of the magnetization as temperature increases, followed by a maximum and a subsequent magnetization decrease. This behavior could be explained as follows [44,45]. At low temperatures, the spin magnetic moment is blocked on its more energetically favorable direction, which is mainly leaded by its anisotropy. However, as temperature increases, the thermal energy become significant to relax spin moment from its easy axis. Thus, the increase described by ZFC curves could be associated to the spin moment relaxation over its energy barrier. Accordingly, is safe to say that this barrier is overcame by the entire particle system at the temperature where ZFC curves exhibit its maximum. This temperature can be related to T_B [44-46]. The correspondent T_B of the 75C25M, 50C50M and 25C75M nanocomposites samples is 44, 78.1, 86.1 K, respectively. As temperature continues to increase above T_B, thermal energy induces the fluctuation of the spin moment orientation between several metastable states. This situation is observed as a decrease of the magnetization, since the spin moments of particles do not follows the applied field when the measure is taken [46].

Moreover, as the M(T) curves of the nanocomposites show (Fig. 4) there is a significant irreversibility between ZFC and FC curves in all cases, and, as the temperature decreases below T_B, FC curves depict an increase on the magnetization above the maximum of the ZFC curves. A possible explanation to this irreversibility could be related to the response of frozen spin moments at the particles surface, which are aligned with the applied field-cooled [45,47]. Under this reasoning, frozen spin moments can also collaborate to increase the magnetization above the maximum of the ZFC curves.

It has been reported that is possible to determine the particles sizes from the initial magnetization data, of magnetic

TABLE I. Particle size distribution calculated from initial magnetitation data.

Parameter	Sample		
	25C75M	50C50M	75C25M
$\overline{d}_v$(nm)	6.01	5.75	5.80
$\overline{d}_a$(nm)	6.88	6.58	6.62
σ_d(s/u)	1.35	1.35	1.34
d_m(nm)	5.25	5.03	5.09
$\overline{d}_n$(nm)	5.49	5.26	5.32
$\overline{d}_{vv}$(nm)	7.19	6.88	6.92

particles under superparamagnetic regime [33,36,48]. This approach involves the use of high field magnetization data, a high field expansion of the Langevin function and to assume a log-normal distribution of particle diameters. Using the reported Eqs. (2)-(7) is possible to calculate [48]: the volume average diameter corresponding to mean crystal volume, $\overline{d}_v$; the diameter corresponding to surface area average diameter, $\overline{d}_a$; log-normal distribution standard deviation, σ_d; the median diameter d_m; the number average diameter, $\overline{d}_n$; and volume weighted average diameter, $\overline{d}_{vv}$.

$$\overline{d}_v = \left[\frac{6k_BTM_0}{\pi M_S C_1}\right]^{\frac{1}{3}} \tag{2}$$

where C_1 and M_0 are the slope and the linear extrapolation to infinite field respectively, from a plot of the observed magnetization (μA-m^2) vs. the inverse field (T^{-1}), k_B is the Boltzmann's constant and T is the temperature at which measurement was performed. The saturation magnetization per unit volume of the crystals presents in the sample, M_S, can be calculated as the ratio of M_0/ε, where ε is the crystalline volume fraction which can be evaluated from the magnetite content and its density (5.2 g/cm^3).

$$\overline{d}_a = \left[\frac{6k_BT}{\pi M_S}\sqrt{\frac{3\chi}{\mu_0 C_1}}\right]^{\frac{1}{3}} \tag{3}$$

where χ is the initial susceptibility in m^3/kg evaluated from the magnetization curve as the slope at zero magnetic field.

$$\sigma_d = \exp\left[\sqrt{\frac{2}{3}\ln\left(\frac{\overline{d}_a}{\overline{d}_v}\right)}\right] \tag{4}$$

$$d_m = \overline{d}_v \exp\left[-\frac{3}{2}\left(\ln\sigma_d\right)^2\right] \tag{5}$$

$$\overline{d}_n = \overline{d}_v \exp\left(-\left(\ln\sigma_d\right)^2\right) \tag{6}$$

$$\overline{d}_{vv} = \overline{d}_v \exp\left(2\left(\ln\sigma_d\right)^2\right) \tag{7}$$

These calculations were performed using the initial magnetization data recorded at 300 K from the nanocomposites samples. The results of the calculations are summarized in Table I. The results are in good agreement with particle sizes obtained from XRD and that observed in TEM images (Fig. 2). Furthermore, these results indicate that particle size is independent of the nanoparticles concentration, even at nanoparticles concentration of 75% w/w.

4. Conclusions

In this work has been reported the preparation of chitosan/magnetite nanocomposites. The proposed synthesis route permits high concentration of stabilized magnetite nanoparticles in a biopolymer matrix (chitosan). Solid state *in situ* co-precipitation using the chitosan as matrix assures narrow particle size distribution of magnetite nanoparticles, whose sizes and standard deviation are independent of magnetite concentration, even at nanoparticles concentration of 75% w/w. These characteristics have not been reached using other reported methods related to the development of chitosan/magnetite nanocomposites.

Acknowledgements

This research was supported by the Programa de Apoyo a la Investigación Científica y Tecnológica (PAICYT) of the Universidad Autónoma de Nuevo León and by the Consejo Nacional de Ciencia y Tecnología (CONACYT). Authors acknowledge the assistance of Profs. R. Escudero and M. José-Yacamán, as well as the support of Dr. U. Ortiz-Méndez.

1. J. Mürbe, A. Rechtenbach, and J. Töpfer, *Mater. Chem. Phys.* **110** (2008) 426.
2. D.-H. Kim, D.E. Nikles, D.T. Johnson, and C.S. Brazel, *J. Magn. Magn. Mater.* **320** (2008) 2390.
3. T.-Y. Liu, S.-H. Hu, S.-H. Hu, S.-P. Tsai, and S.-Y. Chen, *J. Magn. Magn. Mater.* **310** (2007) 2850.
4. A.H. Habib, C.L. Ondeck, P. Chaudhary, M.R. Bockstaller, and M.E. McHenry, *J. Appl. Phys.* **103** (2008) 07A307.
5. J. Lim, R.D. Tilton, A. Eggeman, and S.A. Majestich, *J. Magn. Magn. Mater.* **311** (2007) 78.
6. S.-H. Chung *et al.*, *J. Appl. Phys.* **97** (2005) 10R101.
7. X. Liu *et al.*, *J. Magn. Magn. Mater.* **311** (2007) 84.
8. K. Aurich, M. Schwalbe, J.H. Clement, W. Weitschies, and N. Buske, *J. Magn. Magn. Mater.* **311** (2007) 1.

9. A. Zhu, L. Yuan, and T. Liao, *Int. J. Pharm.* **350** (2008) 361.
10. Z. Bo, X. Jianmin, and L. Huizhou, *Front. Chem. Eng. Chin.* **1** (2007) 96.
11. T. Neuberger, B. Schöpf, H. Hofmann, M. Hofmann, and B.V. Rechenberg, *J. Magn. Magn. Mater.* **293** (2005) 483.
12. J. Giri *et al.*, *J. Magn. Magn. Mater.* **320** (2008) 724.
13. P. Pradhan, J. Giri, R. Banerjee, J. Bellare, and D. Bahadur, *J. Magn. Magn. Mater.* **311** (2007) 208.
14. Q.A. Pankhurst, J. Connolly, S.K. Jones, and J. Dobson, *J. Phys. D: Appl. Phys.* **36** (2003) R167.
15. B.Y. Kularatne *et al.*, *Cytometry* **50** (2002) 160.
16. S. Morisada, N. Miyata, and K. Iwahori, *J. Microbiol. Methods* **51** (2002) 141.
17. S.S. Andrade, D. Rabelo, V.K. Garg, A.C. Oliveira, and P.C. Morais, *J. Magn. Magn. Mater.* **289** (2005) 25.
18. R.A. Ali-zade, *J. Colloids and Surfaces A: Physicochem. Eng. Aspects* **225** (2005) 111.
19. Z. Huang and F. Tang, *J. Colloid and Interface Sci.* **275** (2004) 142.
20. D. Rabelo *et al.*, *Nano lett.* **1** (2001) 105.
21. V. Belessi *et al.*, *Chem. Mater.* **20** (2008) 3298.
22. A. Zhu, L. Yuan, and T. Liao, *Int. J. Pharm.* **350** (2008) 361.
23. K. Donadel *et al.*, *Mater. Sci. Eng., C* **28** (2008) 509.
24. E.H. Kim, Y. Ahnb, and H.S. Lee, *J. Alloys Compd.* **434** (2007) 633.
25. E. Onsoyen and O. Skaugrud, *J. Chem. Technol. and Biotechnol.* **49** (1990) 345.
26. J.R. Deans and B.G. Dixon, *Water Res.* **26** (1992) 469.
27. G.L. Rorrer, T.-Y. Hsien, and J.D. Way, *Ind. Eng. Chem. Res.* **32** (1993) 2170.
28. W. Kaminski and Z. Modrzejewska, *Sep. Sci. Technol.* **32** (1997) 2659.
29. R. Schmuhl, H. M. Krieg, and K. Keizer, *Water SA* **27** (2001) 1.
30. A. Burke, E. Yilmaz, and N. Hasirci, *Turk. J. Med. Sci.* **30** (2000) 341.
31. L. Jin and R. Bai, *Langmuir* **18** (2002) 9765.
32. A.K. Boal, K. Das, M. Gray, and V.M. Rotello, *Chem. Mater.* **14** (2002) 2628.
33. B. Li, D. Jia, Y. Zhou, Q. Hu, and W. Cai, *J. Magn. Magn. Mater.* **306** (2006) 223.
34. M. Garza-Navarro *et al.*, *J. Appl. Polym. Sci.* (2009) DOI: 10.1002/app.31043.
35. D. Cheng, X. Zhou, H. Xia, and H. Chan, *Chem. Mater.* **17** (2005) 3578.
36. C. Jung and P. Jacobs, *Magn. Resonan. Imaging* **13** (1995) 661.
37. J.L. López, H.-D. Pfannes, R. Paniago, J.P. Sinnecker, and M.A. Novak, *J. Magn. Magn. Mater.* **320** (2008) e327.
38. K. Maaz, A. Mumtaz, S.K. Hasanain, and A. Ceylan, *J. Magn. Magn. Mater.* **308** (2007) 289.
39. R. Cornell and U. Schwertmann, *The iron oxides: structure, properties, reactions, occurrences and uses*, (Wiley-VCH Verlag GmbH & Co. KGaA, Weinheim, 2003).
40. R. Sato Turtelli, G. V. Duong, W. Nunes, R. Grössinger, and M. Knobel, *J. Magn. Magn. Mater.* **320** (2008) e339.
41. R.H. Kodama, *J. Magn. Magn. Mater.* **200** (1999) 359.
42. J.M.D. Coey, *Phys. Rev. Lett.* **27** (1971) 1140.
43. D.S. Mathew and R.-S. Juang, *Chem. Eng. J.* **219** (2007) 51.
44. D.L. Leslie-Pelecky and R.D. Rieke, *Chem. Mater.* **8** (1996) 1770.
45. A. Labarta, X. Batlle, and O. Iglesias, *From finite size and surface effects to glassy behaviour in ferrimagnetic nanoparticles*, chapter 4 in the book: *"Surface effects in magnetic nanoparticles"* (D. Fiorani, editor, Nanostructured Science and Technology Series, Spinger Science+Business, Inc., Nueva York, 2005).
46. K.M. Unruh and C.L. Chien, *Magnetic and electron transport properties of granular films*, chapter 14 of the book: "*Nanomaterials: synthesis, properties and applications"*, (A. S. Edelstein, R. C. Cammarata, editors, Series in Micro and Nanoscience and Technology, Institute of Physics Publishing, London, 2002).
47. B. Martínez, X. Obradors, Ll. Balcells, A. Rouanet, and C. Monty, *Phys. Rev. Lett.* **80** (1998) 181.
48. C.E. Sjögren *et al.*, *Magn. Reson. Imaging* **15** (1997) 55.